J. Plasma Physics (2009), *vol.* 75, *part* 1, *pp.* 53–69.
doi:10.1017/S0022377808007204 Printed in the United Kingdom

Numerical prediction of the saturation limit of atmospheric pressure AC dielectric barrier discharges

KHALIL ARSHAK, IVOR GUINEY and EDWARD FORDE

Department of Electronic and Computer Engineering, University of Limerick, Limerick, Ireland (ivor.guiney@ul.ie)

(Received 31 October 2007 and accepted 20 February 2008, first published online 18 April 2008)

Abstract. In this paper the evolution of species densities up to the saturation limit in pulsed dielectric barrier discharges in atmospheric air plasma is predicted. The saturation limit itself is presented in the form of an exponential equation and is validated by computer modeling of continuity equations and atmospheric reactions coupled with appropriate dielectric dependent boundary conditions. Microdischarge streamer times are treated independently and a profile of the species generation due to all microdischarges within the plasma is presented. Quasi-neutrality is assumed for calculations and a theoretical maximum value for species densities in such a plasma is additionally outlined. Results show a good agreement between simulated and calculated values and serve to illustrate the onset of saturation in atmospheric pressure plasmas in general. Practical conditions of voltage, gap distance and frequency are incorporated so as to make the model as realistic as possible.

1. Introduction

In recent years much time has been spent researching the physics of plasmas controlled by dielectric barriers. This can be attributed to the fact that plasmas are becoming more relevant in engineering and science. Applications of plasmas now include surface modification, ozone production, thin-film deposition, etching and sterilization of bacteria—topics that have only been strongly investigated recently. For the majority of working gases and discharge conditions, the barrier discharge consists of numerous filaments about 10 ns in duration, which are, as a rule, stochastically distributed over the electrode surface. Various polymers such as polypropylene and polyesters have been investigated when treated by plasmas [1–3] and results such as an improvement in surface wettability have been recorded.

A modeling process capable of predicting the evolution of charged species within a plasma system, and hence the limit of saturation of these species, is developed in this paper. The model is based upon a simultaneous solution of the continuity equations for charged and excited particles, and the Poisson equation [4] coupled with previously unconsidered atmospheric reactions. Quantities such as mobility, diffusion coefficient, and ionization rate characterize the processes in a discharge volume. These values are well known. The interaction between plasma and a dielectric

surface is usually insignificant and therefore the surface processes are not taken into account. In this paper a new saturation limit equation is derived and compared with results obtained from computer modeling of the above method. The theoretical maximum species density is established and is applicable to all gases.

2. Dielectric barrier discharge equations

In this section, a system of equations describing the homogeneous barrier discharge in atmospheric air is formulated according to equations laid out previously [4]. This theory is reviewed and new atmospheric reactions are incorporated into the continuity equations for electrons and ions respectively. The discharge current is only limited by dielectric barriers; there is no external resistance. The discharge is supplied by the external voltage $U_{\text{ext}}(t)$, which is an input parameter of the model.

The charged particles (electrons and ions) are described by the continuity equations

$$\frac{\delta n_{\text{e}}}{\delta t} - b_{\text{e}}\left(E\nabla\cdot n_{\text{e}} + \frac{T_{\text{e}}}{e}\nabla^2\cdot n_{\text{e}}\right) = n_{\text{e}}\nu_{\text{ion}} - \alpha_{\text{rec}} n_{\text{i}} n_{\text{e}} + \sum_j k_j n_q n_r, \tag{2.1}$$

$$\frac{\delta n_{\text{i}}}{\delta t} - b_{\text{i}}\left(-E\nabla\cdot n_{\text{i}} + \frac{T_{\text{i}}}{e}\nabla^2\cdot n_{\text{i}}\right) = n_{\text{e}}\nu_{\text{ion}} - \alpha_{\text{rec}} n_{\text{i}} n_{\text{e}} + \sum_j k_j n_q n_r, \tag{2.2}$$

where $n_{\text{e(i)}}$ are the densities of electrons and ions, respectively, $T_{\text{e(i)}}$ are the kinetic temperatures of electrons and ions, respectively, $b_{\text{e(i)}}$ are the mobilities of electrons and ions, respectively, E is the axial electric field, ν_{ion} is the frequency of direct ionization, and $\alpha_{\text{rec}} = 1.1\times10^{-7} T_{\text{i}}^{-0.5}\ \text{cm}^3\ \text{s}^{-1}$ is the coefficient of dissociative recombination [5]. The values b_{e}, T_{e}, and ν_{ion} are assumed to be functions of the local electric field. They are determined by the electron distribution function, which is obtained from the Boltzmann kinetic equation using a numerical Boltzmann equation solver, BOLSIG [6]. The atmospheric reactions in the above equations are calculated using the rate coefficients for the given reactions in Table 1 where k_j is the rate coefficient of reaction j in Table 1 and n_q and n_r are the densities of the respective species q and r in reaction j. The product of the rate coefficients with the respective densities of the species present will allow these reactions to be included in the continuity equations above.

The surface densities of charged particles at both dielectric barriers are described by the following equations:

$$\frac{d\sigma_{\text{e}}}{dt} = n_{\text{e}} v_{\text{e}} - \sigma_{\text{e}}\nu_{\text{e}}^{\text{des}} - \alpha_{\text{rw}}\sigma^{+}\sigma_{\text{e}}, \tag{2.3}$$

$$\frac{d\sigma^{+}}{dt} = (1+\gamma) n_{\text{i}} v_{\text{i}} - \alpha_{\text{rw}}\sigma^{+}\sigma_{\text{e}}, \tag{2.4}$$

where σ_{e} is the electron surface density, σ^{+} is the surface density of positive charge, $v_{\text{e(i)}}$ have the sense of thermal velocity of particles, $\nu_{\text{e}}^{\text{des}}$ is the electron desorption frequency, γ is the ion–electron emission coefficient (taken to be 0.01 [4]), and α_{rw} is a recombination rate constant. The electric field in the volume is described by the Poisson equation

$$\nabla\cdot E = \frac{\rho}{\epsilon}, \tag{2.5}$$

https://doi.org/10.1017/S0022377808007204 Published online by Cambridge University Press

Table 1. Atmospheric reactions considered in the kinetic model.

Reaction number	Reaction	Rate constant ($cm^3\ s^{-1}$)	Reference
1	$N_2^* + N_2 \rightarrow N_2 + N_2$	1.9×10^{-13}	[7]
2	$N_2^* + O_2 \rightarrow O + O + N_2$	1.5×10^{-12}	[7]
3	$O_2^* + O_3 \rightarrow O + O_2 + O_2$	$5.2 \times 10^{-11} \exp(-2840/T)^{\dagger}$	[8]
4	$O_2^* + N_2 \rightarrow O_2 + N_2$	$3.0 \times 10^{-18} \exp(-200/T)$	[9]
5	$N_2^+ + N_2 + M^{\ddagger} \rightarrow$	1.1×10^{-29}	[10]
6	$N_2^+ + O_2 \rightarrow O_2^+ + N_2$	5.1×10^{-11}	[10]
7	$N_2^+ + H_2O \rightarrow H_2O^+ + N_2$	2.0×10^{-9}	[11]
8	$N_4^+ + O_2 \rightarrow O_2^+ + N_2 + N_2$	2.5×10^{-10}	[10]
9	$O_2^+ + H_2O + M \rightarrow O_2 + H_2O + M$	2.5×10^{-28}	[10]
10	$O_2^+ \cdot H_2O + H_2O \rightarrow H_3O^+ + OH + O_2$	1.2×10^{-9}	[10]
11	$H_2O^+ + H_2O \rightarrow H_3O^+ + OH$	1.7×10^{-9}	[10]
12	$H_3O^+ + H_2O + M \rightarrow H_3O^+ \cdot H_2O + M$	5.0×10^{-27}	[10]
13	$O_2^- + H_3O^+ \cdot H_2O \rightarrow O_2 + H + H_2O + H_2O$	2.0×10^{-6}	[10]
14	$O_2^- + O_2^+ \cdot H_2O \rightarrow O_2 + O_2 + H_2O$	2.0×10^{-6}	[10]
15	$N + OH \rightarrow NO + H$	$3.8 \times 10^{-11} \exp(85/T)$	[12]
16	$N + NO \rightarrow N_2 + O$	$3.4 \times 10^{-11} \exp(-24/T)$	[13]
17	$N + O_2 \rightarrow NO + O$	$4.4 \times 10^{-12} \exp(-3220/T)$	[12]
18	$O + O_2 + M \rightarrow O_3 + M$	$3.4 \times 10^{-34} (T/298)^{-1.2}$	[13]
19	$O + HO_2 \rightarrow OH + O_2$	$2.9 \times 10^{-11} \exp(-200/T)$	[12]
20	$O + OH \rightarrow H + O_2$	$2.3 \times 10^{-11} \exp(110/T)$	[14]
21	$O + O_3 \rightarrow O_2 + O_2$	$8.0 \times 10^{-12} \exp(-2060/T)$	[12]
22	$H + O_3 \rightarrow OH + O_2$	$1.4 \times 10^{-10} \exp(-470/T)$	[13]
23	$O_2^+ \cdot H_2O + H_2O \rightarrow H_3O^+ + OH + O_2$	1.2×10^{-9}	[10]
24	$O + HO_2 \rightarrow OH + O_2$	$2.9 \times 10^{-11} \exp(200/T)$	[13]
25	$OH + HO_2 \rightarrow H_2O + O_2$	8.0×10^{-11}	[13]
26	$OH + O_3 \rightarrow HO_2 + O_2$	$1.9 \times 10^{-12} \exp(-1000/T)$	[15]
27	$OH + NO_2 + M \rightarrow HNO_3 + M$	$2.2 \times 10^{-30} (T/298)^{-2.9}$	[13]
28	$H + O_2 + M \rightarrow HO_2 + M$	$1.8 \times 10^{-32} (T/298)^{-0.8}$	[16]
29	$HO_2 + HO_2 + M \rightarrow H_2O_2 + O_2 + M$	$1.9 \times 10^{-33} \exp(980/T)$	[9]
30	$OH + OH + M \rightarrow H_2O_2 + M$	$6.9 \times 10^{-31} (T/298)^{-0.8}$	[9]
31	$H_2O_2 + OH \rightarrow H_2O + HO_2$	$2.9 \times 10^{-12} \exp(-160/T)$	[9]
32	$O + NO_2 \rightarrow NO + O_2$	$6.5 \times 10^{-13} \exp(180/T)$	[12]
33	$NO + O_3 \rightarrow NO_2 + O_2$	$4.3 \times 10^{-12} \exp(-1598/T)$	[17]
34	$NO + OH + M \rightarrow HNO_2 + M$	$8.6 \times 10^{-31} \exp(34/T)$	[18]
35	$NO + HO_2 \rightarrow NO_2 + OH$	$3.5 \times 10^{-12} \exp(240/T)$	[17]
36	$OH + HNO_2 \rightarrow NO_2 + H_2O$	$1.8 \times 10^{-11} \exp(-390/T)$	[13]
37	$NO_2 + N \rightarrow N_2O + O$	2.4×10^{-11}	[10]
38	$NO_2 + O + M \rightarrow NO_3 + M$	$9.0 \times 10^{-32} (T/298)^{-2.0}$	[13]
39	$OH + HNO_3 \rightarrow NO_3 + H_2O$	$1.5 \times 10^{-14} \exp(650/T)$	[15]
40	$NO_3 + NO_2 + M \rightarrow N_2O_5 + M$	$10^{-30} (T/298)^{-3.4}$	[12]

†T in all reactions refers to gas temperature in Kelvin.
‡M in all reactions refers to major species acting as a third body in three-body collision reactions.

where ρ is the charge density and ϵ is the dielectric permittivity. Integration of this equation in x, using a fourth-order Runge–Kutta algorithm, whilst taking into account the surface charges, yields

$$E(x,t) = 4\pi q_{\text{ext}}(t) + 4\pi e\left[\sigma_0^+(t) - \sigma_{\text{e}0}(t) + \int_0^L (n_{\text{i}}(x',t) - n_{\text{e}}(x',t))\,dx'\right] \qquad (2.6)$$

where $\sigma_{\text{e}0}$ and σ^+ are the initial surface densities of electrons and positive charge, respectively, q_{ext}(t) is the surface charge at the external metal electrode, and L is the length of the inter-electrode gap. The surface area of charge deposition is assumed to be equal to the diameter of the filamentary discharges given by [19].

The system of equations (2.1)–(2.6) describes the homogeneous barrier discharge completely as the profile of external voltage is given. This system is solved numerically, and the calculation is carried out for the sinusoidal external voltage

$$U_{\text{ext}}(t) = U_0 \sin(2\pi t/T)$$

https://doi.org/10.1017/S0022377808007204 Published online by Cambridge University Press

up to the establishment of the periodic solution. T represents the period of the applied AC voltage.

3. Saturation limit of atmospheric air plasma

Due to the fact that the microdischarges occurring within a dielectric barrier discharge (DBD) plasma exist for tens of nanoseconds, the plasma will have reached its theoretical maximum density within the first AC high-voltage pulse applied to the system. Thus, the number of charged species (electrons or ions) created over the course of the first applied voltage pulse can be broken down into those charged species created by ionization due to the electric field minus those which have recombined within the plasma volume [20]. In this section we derive a formula which predicts the gain of the charged species within a plasma volume up to a maximum limit. For this we assume quasi-neutrality, i.e. that $n_e = n_i = n$. From the basic continuity equation we have

$$n(t) = \int (n_{\text{ionization}} - n_{\text{recombination}})\, dt \tag{3.1}$$

where $n_{\text{ionization}}$ is the species number density generated by ionization, $n_{\text{recombination}}$ the number density of species that have recombined, when considered over time, and $n(t)$ is the total net quantity of species generated. This can be expressed as

$$\frac{d}{dt} n(t) = n(t)\nu_{\text{ion}} - n(t)^2 \alpha_{\text{rec}}. \tag{3.2}$$

Integration of this equation between the limits of initial density n_0 and density after a time τ, n_τ yields

$$\int_{n_0}^{n_\tau} \frac{1}{n(1 - n(\alpha_{\text{rec}}/\nu_{\text{ion}}))}\, dn = \nu_{\text{ion}} \cdot \tau, \tag{3.3}$$

where τ is a dummy variable in time. Solving this results in the following equation:

$$\ln\left(\frac{n_\tau}{n_0}\right) - \ln\left[\frac{(-\nu_{\text{ion}}) + n_\tau \cdot \alpha_{\text{rec}}}{(-\nu_{\text{ion}}) + n_0 \cdot \alpha_{\text{rec}}}\right] = \nu_{\text{ion}} \cdot \tau \tag{3.4}$$

and solving for n_τ gives

$$n_\tau = \exp(\nu_{\text{ion}} \cdot \tau)\left[\frac{\nu_{\text{ion}}}{\nu_{\text{ion}} - n_0 \alpha_{\text{rec}} + \exp(\nu_{\text{ion}} \cdot \tau) n_0 \alpha_{\text{rec}}}\right] n_0. \tag{3.5}$$

Defining a saturation limit of ion density, $n_{\max}$,

$$n_{\max} = \frac{\nu_{\text{ion}}}{\alpha_{\text{rec}}}, \tag{3.6}$$

the final result is obtained,

$$n_\tau = \frac{n_{\max}}{((n_{\max}/n_0) - 1)\exp[-n_{\max}\alpha_{\text{rec}}\tau] + 1}. \tag{3.7}$$

https://doi.org/10.1017/S0022377808007204 Published online by Cambridge University Press

For the purposes of calculation and validation of simulation with theory, the following formulae were used for ionization and recombination coefficients:

$$\nu_{\text{ion}} = A\frac{g_{\text{i}}}{g_0}\frac{me^{10}}{\hbar^3 T_{\text{e}}^3}\exp\left(-\frac{I}{T_{\text{e}}}\right), \tag{3.8}$$

$$\alpha_{\text{rec}} = w_{\text{a}0}\left(\frac{2\pi\hbar}{mT}\right)^{3/2}\frac{\Gamma T}{2\pi\epsilon_{\text{a}}^2}, \tag{3.9}$$

where A is a proportionality factor of the order of unity, g_{i} and g_0 are the statistical weights of the ion and neutral gas respectively, m is the mass of an electron, I is the ionization potential of a ground state ion, $w_{\text{a}0}$ is the frequency of transitions from the autoionized state to the bound state, T is the gas temperature in Kelvin, Γ is the width of the autoionization level, and ϵ_{a} is the excitation energy. Derivations of the above equations can be found in [21] and we assume that recombination proceeds via the formation of an autoionized atomic state [22].

This equation describes the build-up of species depending on how long the plasma is in operation. Knowing key commodities such as ionization frequency and recombination coefficient, it is possible to determine accurately how long it takes for a specific species density to be obtained.

An alternative method to this is to use numerical integration to solve equation 3.1 in conjunction with a similar equation describing electron number density build-up, i.e.

$$n_{\text{i}}(t) = \int_{n_{\text{i initial}}}^{n_{\text{i max}}} (\nu_{\text{ion}} n_{\text{i}}(t) - \alpha_{\text{rec}} n_{\text{e}}(t) n_{\text{i}}(t))\, dt, \tag{3.10}$$

$$n_{\text{e}}(t) = \int_{n_{\text{e initial}}}^{n_{\text{e max}}} (\nu_{\text{ion}} n_{\text{e}}(t) - \alpha_{\text{rec}} n_{\text{e}}(t) n_{\text{i}}(t))\, dt. \tag{3.11}$$

Assuming standard initial conditions of unity for both electron and ion number densities, integration can be carried out until convergence is reached.

4. Results and discussion

Graphs of the species densities of the first nine time periods corresponding up to 90 ns can be seen in Figs 1–18. Further simulations were not carried out due to the fact that the plasma had by this time saturated. The operating conditions were for an applied AC voltage of 10 kV peak-to-peak operating at 10 kHz (the period width is 0.1 ms) for an electrode gap of 0.3 cm with a dielectric width of 6.8×10^{-3} cm [23], where the overall increase of species over this timestep is taken into account. These represent the evolution of charged particles upon the application of a high-voltage AC pulse to the dielectric covered electrodes. Values for the frequency of ionization and recombination coefficient are the same as those outlined in Sec. 2 and air is taken to be the working gas.

Figures 1 and 2 describe the evolution of charged species upon application of the first high-voltage pulse to the system. Exponential increase is in evidence, with the respective species tending to accumulate towards the electrode of opposite polarity to their respective charges. Similar exponential increase is observed in Figs 3 and 4. The densities here are much greater than in Figs 1 and 2, however, due to the fact that the initial densities for this time period are considerably higher than for

https://doi.org/10.1017/S0022377808007204 Published online by Cambridge University Press

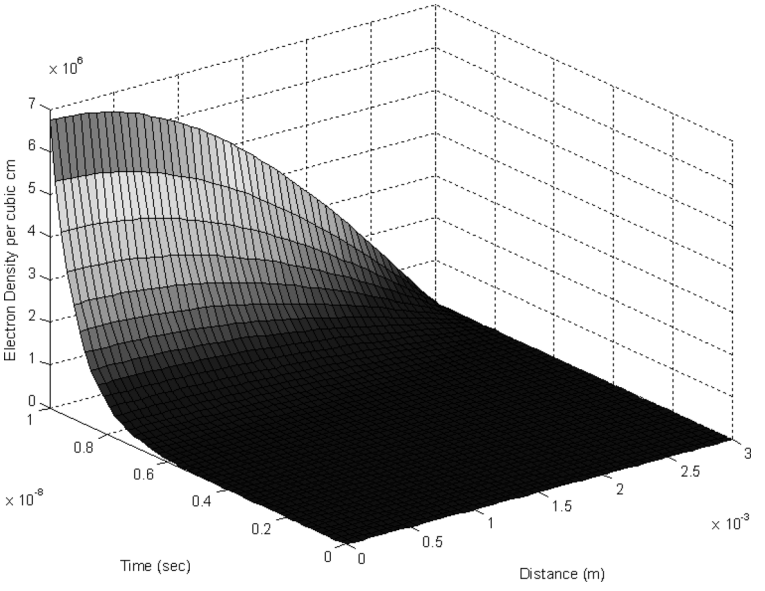

Figure 1. Electron density at 10 ns.

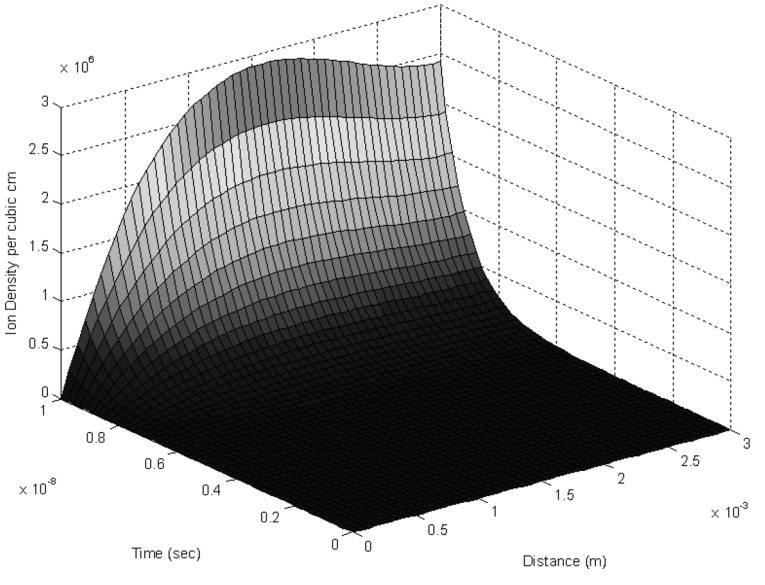

Figure 2. Ion density at 10 ns.

system initiation. Once more, the charged species tend to accumulate towards the electrode of opposite polarity to their respective charge. However, the ion density falls off slightly towards the negative cathode. This can be explained by the fact that upon this pulse the heavier ions do not have sufficient energy to traverse the final electrostatic sheath and thus recombine as efficiently at the negative cathode.

Figures 5–8 show the evolution of species for the third and fourth time periods respectively, i.e. between 20 and 40 ns. It is interesting to note that even at this

https://doi.org/10.1017/S0022377808007204 Published online by Cambridge University Press

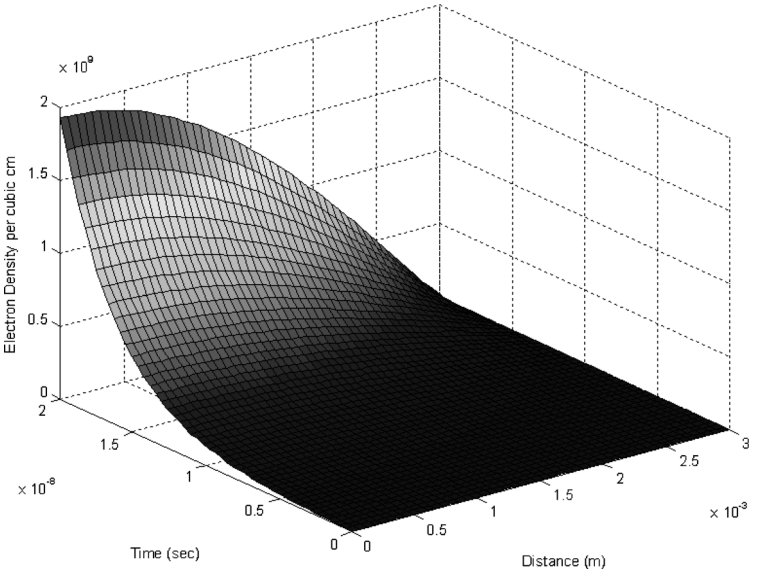

Figure 3. Electron density at 20 ns.

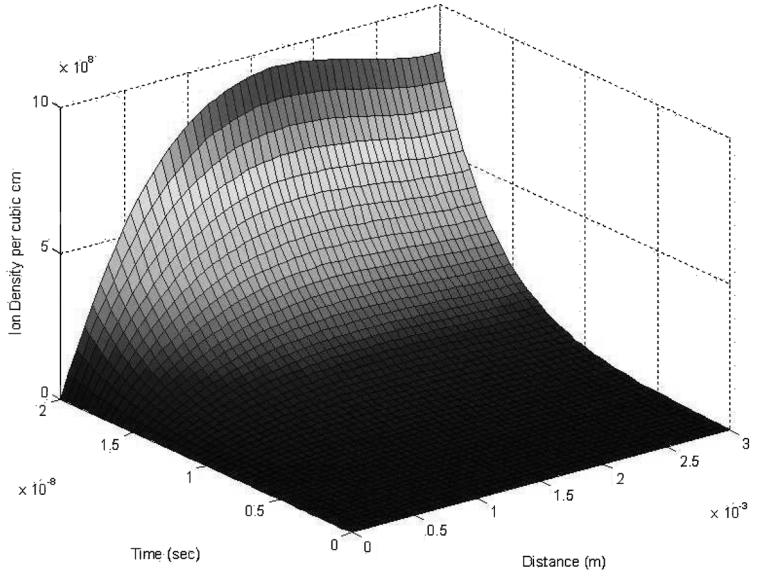

Figure 4. Ion density at 20 ns.

early stage of plasma formation the onset of saturation is just commencing. These graphs predominantly exhibit a logarithmic increase over an exponential increase due to the fact that the air is becoming 'swamped' with charged species. This is particularly in evidence from Fig. 8, where the logarithmic increase is very small after the initial jump to a higher level of ionic density.

Figures 9–12 illustrate the respective species densities between 40 and 60 ns. Again, due to the rise in initial density conditions, the initial jump to a higher

https://doi.org/10.1017/S0022377808007204 Published online by Cambridge University Press

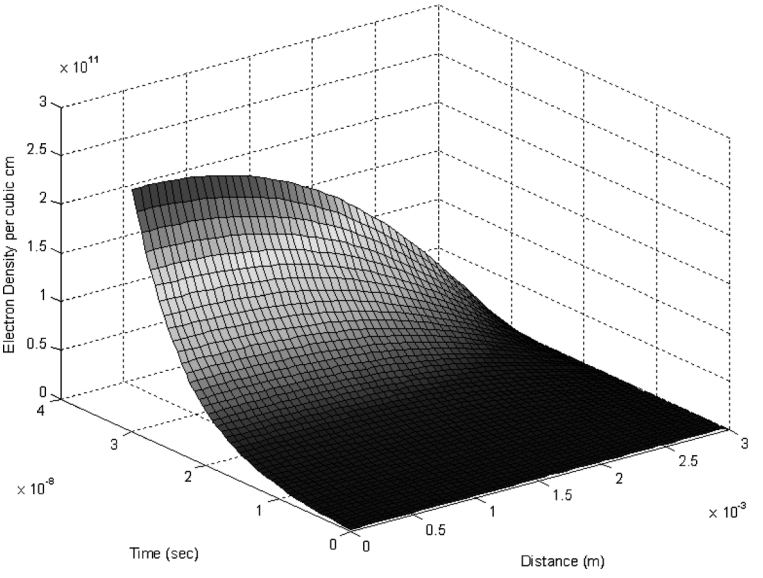

Figure 5. Electron density at 30 ns.

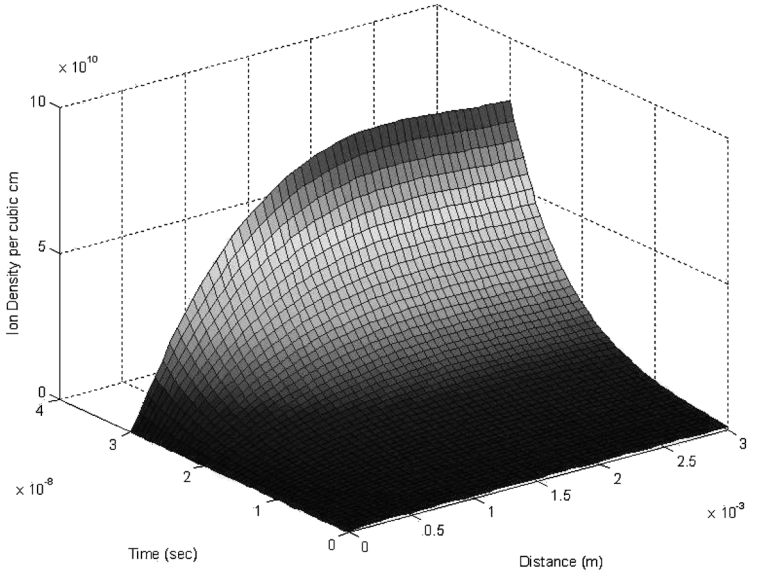

Figure 6. Ion density at 30 ns.

species density is quite abrupt before the concentration tends to level out. The shape of these graphs is similar to Figs 13–16, where a logarithmic increase is again clearly visible. It should be noted that decay of both ions and electrons still occurs at the respective electrode of opposite polarity even when coupled with overall increase in the system. The graphs also show that the overall species density is gradually becoming greater, albeit at a much slower rate than previously observed. This illustrates the fact that, in addition to individual time steps producing a limiting

https://doi.org/10.1017/S0022377808007204 Published online by Cambridge University Press

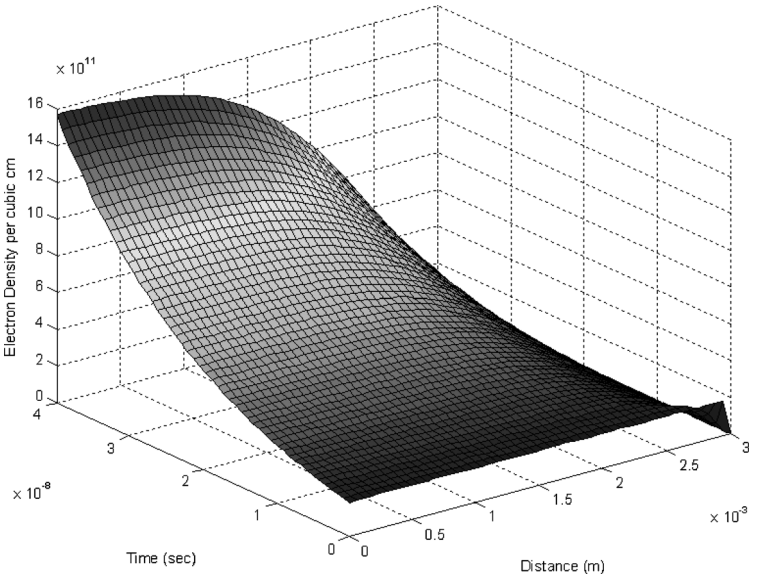

Figure 7. Electron density at 40 ns.

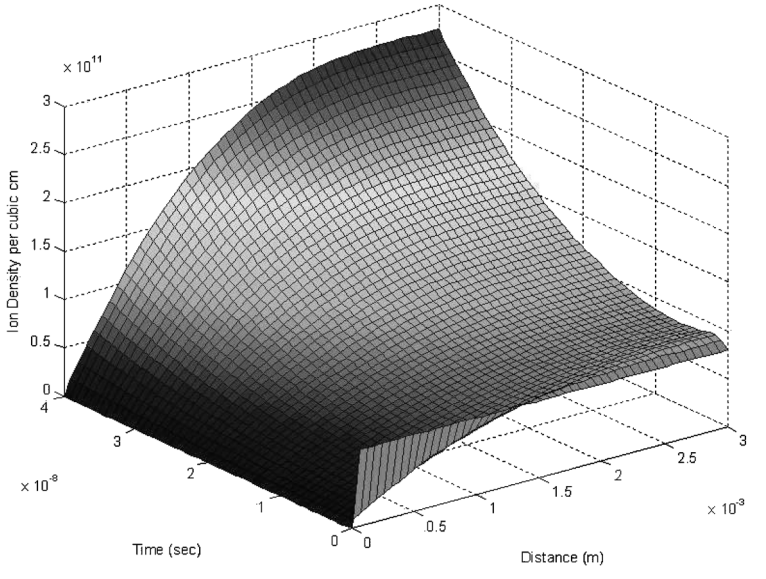

Figure 8. Ion density at 40 ns.

increase after the application of multiple pulses, the overall gain of the system exhibits a limiting increase also.

The ninth pulse modeled in Figs 17 and 18 shows that saturation is dominant by this time. Figure 18 in particular shows only minuscule increases in species density as opposed to its predecessor (Fig. 16). While small increases in species densities will continue to be in evidence subsequent to this pulse, the overall limit will remain reasonably static.

https://doi.org/10.1017/S0022377808007204 Published online by Cambridge University Press

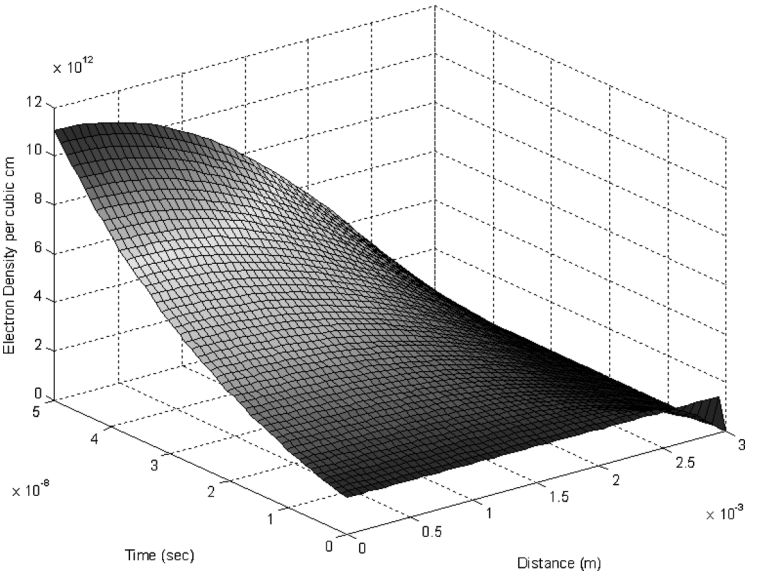

Figure 9. Electron density at 50 ns.

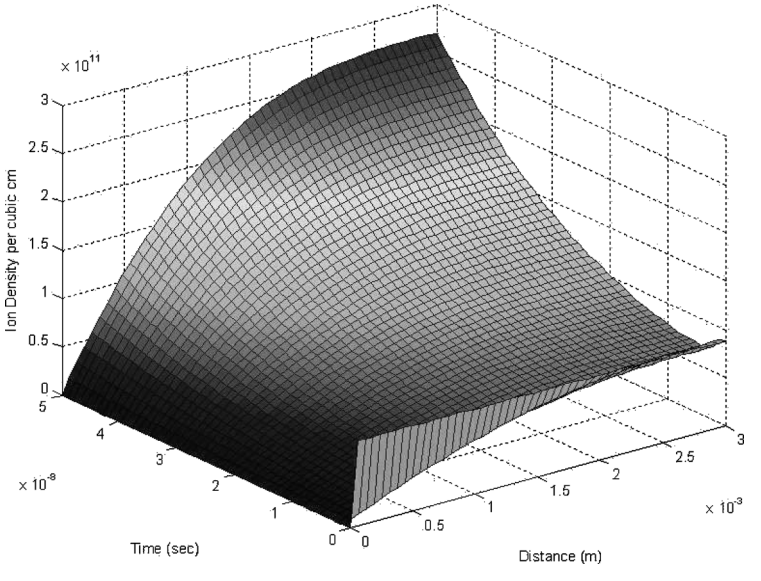

Figure 10. Ion density at 50 ns.

Figure 19 shows the overall species densities for electrons and ions, respectively. The value for the maximum number densities for electrons and ions was obtained from [24] and was incorporated in the calculation of how the active species in a plasma approach saturation 3.1. The theoretical density of ions has been calculated using values obtained in Sec. 2 and applying them to 3.1. As can be seen, the results of the modeled and theoretical ion densities correspond very closely to one another with very little error in evidence.

https://doi.org/10.1017/S0022377808007204 Published online by Cambridge University Press

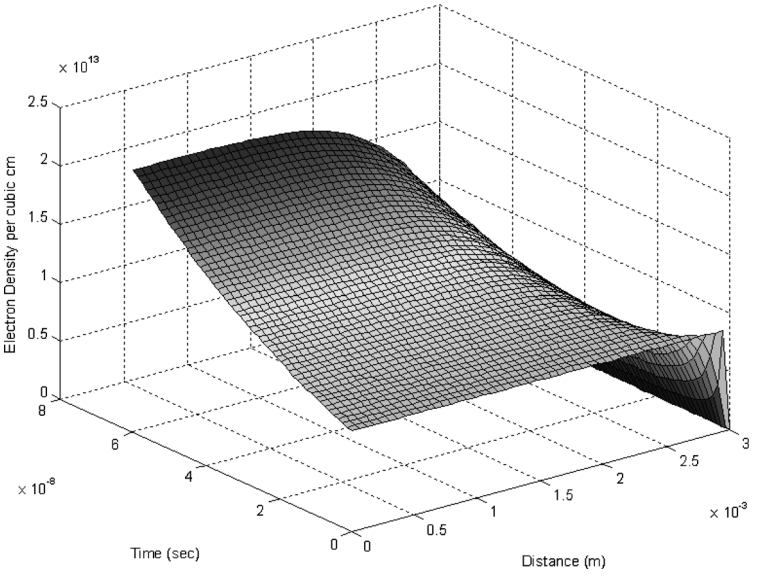

Figure 11. Electron density at 60 ns.

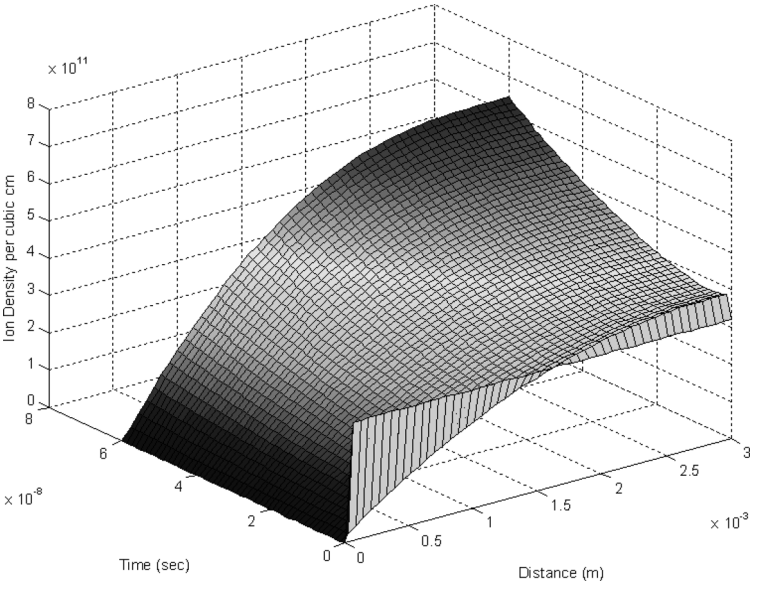

Figure 12. Ion density at 60 ns.

These active species are primarily generated on the occurrence of a typical current spike of the plasma of interest. Each of the active species (electrons and ions) will emit a small amount of light which can be detected with a photomultiplier tube. This is outlined in Fig. 20, which shows the unrectified light output increasing suddenly on the occurrence of a current spike [25].

Even though the model is plausible for atmospheric air, the overall species densities may be slightly erroneous due to the lack of accurate experimental data

https://doi.org/10.1017/S0022377808007204 Published online by Cambridge University Press

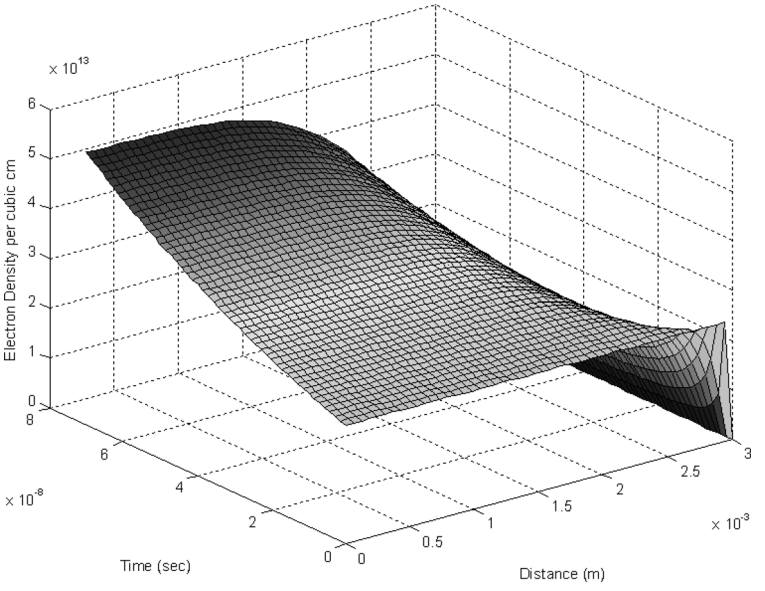

Figure 13. Electron density at 70 ns.

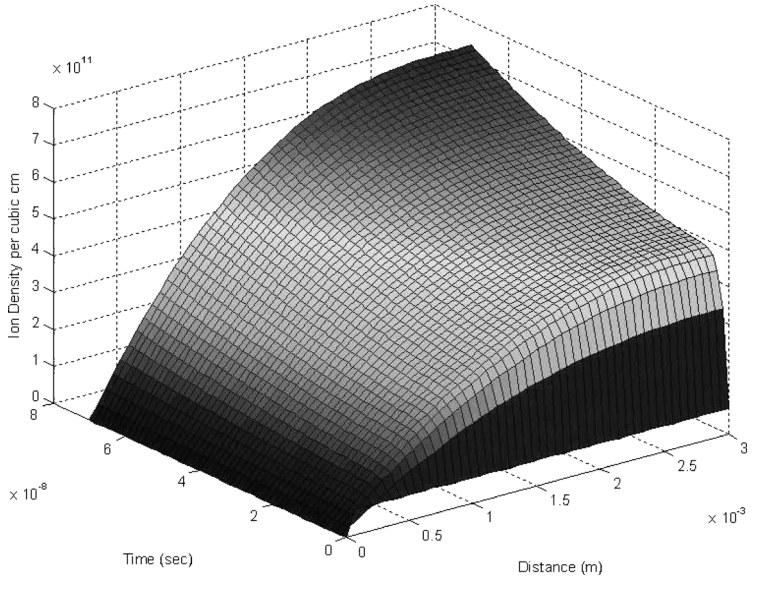

Figure 14. Ion density at 70 ns.

regarding species densities in air plasma. Future work on this topic will focus on spectroscopic techniques to obtain accurately initial densities for all atmospheric reactions considered [26]. Some of the rate constants outlined in Table 1 of this paper lack temperature dependence which would make them more accurate at all temperatures and atmospheric pressures. This would not be an issue for metastables of different species but could conceivably affect ionic formation. Due to the lack

https://doi.org/10.1017/S0022377808007204 Published online by Cambridge University Press

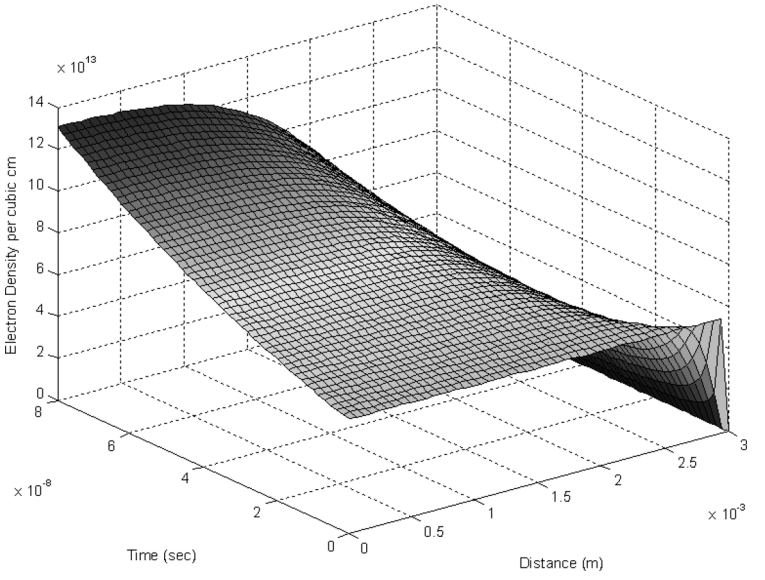

Figure 15. Electron density at 80 ns.

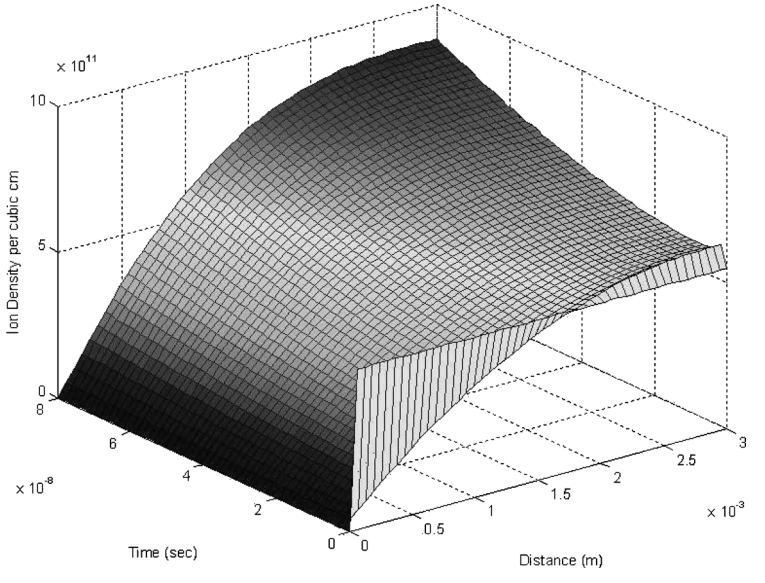

Figure 16. Ion density at 80 ns.

of this data, the rate constants utilized are as accurate as possible at this time. However, as a possible hypothesis, it is interesting to investigate the importance of other processes for the existence of a homogeneous discharge.

Over a longer timescale, more than one-dimensional effects, such as radial diffusion, heat transfer, etc., are necessary for the calculations of the evolution of the respective species densities. Implementation of theory such as that found in [27]

https://doi.org/10.1017/S0022377808007204 Published online by Cambridge University Press

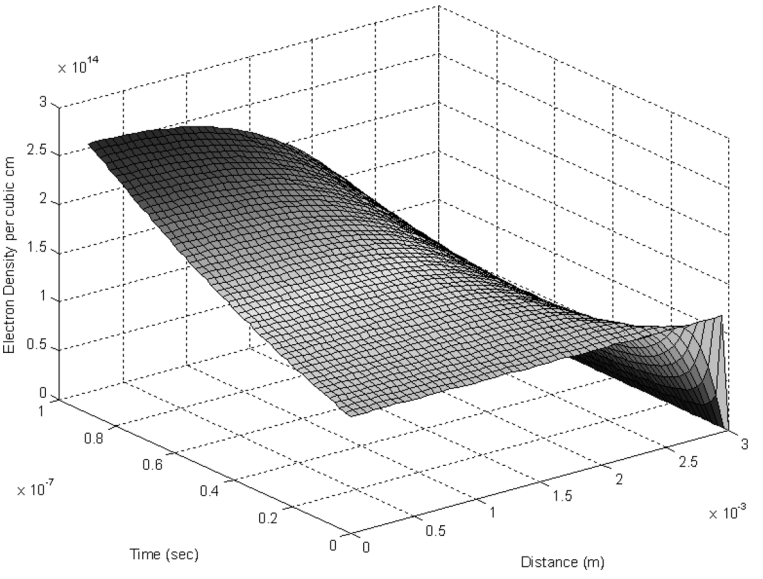

Figure 17. Electron density at 90 ns.

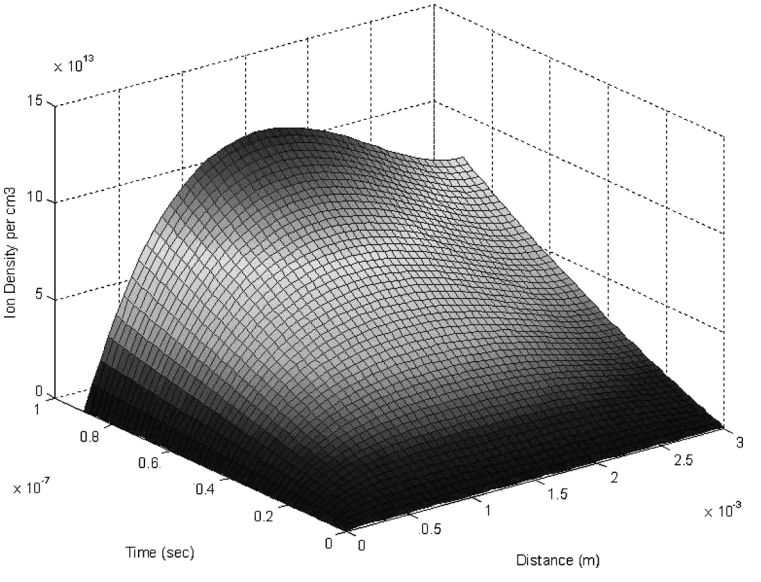

Figure 18. Ion density at 90 ns.

would result in a more accurate modeling of the build-up of charged species in the DBD configuration. This is planned for future work.

Accuracy of the Poisson equation could further be improved upon by implementing a higher-order Runge–Kutta algorithm when employing iteration methods in (2.1)–(2.6). This would be extremely computationally intensive and thus was not integrated in our calculations. Future study is proposed in this area, in conjunction

https://doi.org/10.1017/S0022377808007204 Published online by Cambridge University Press

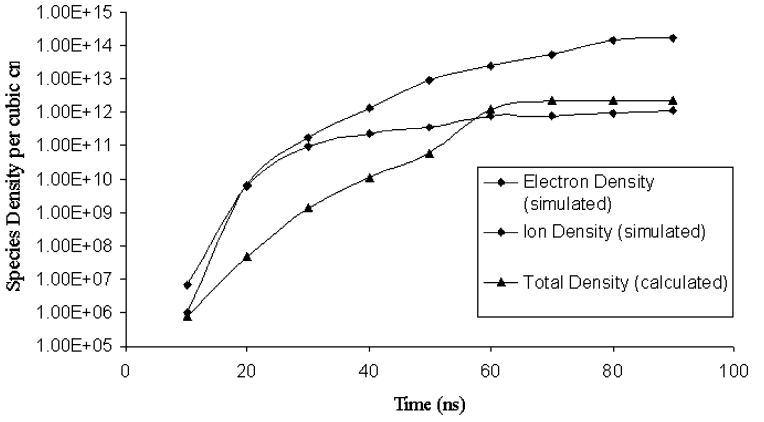

Figure 19. Electron and ion densities with time.

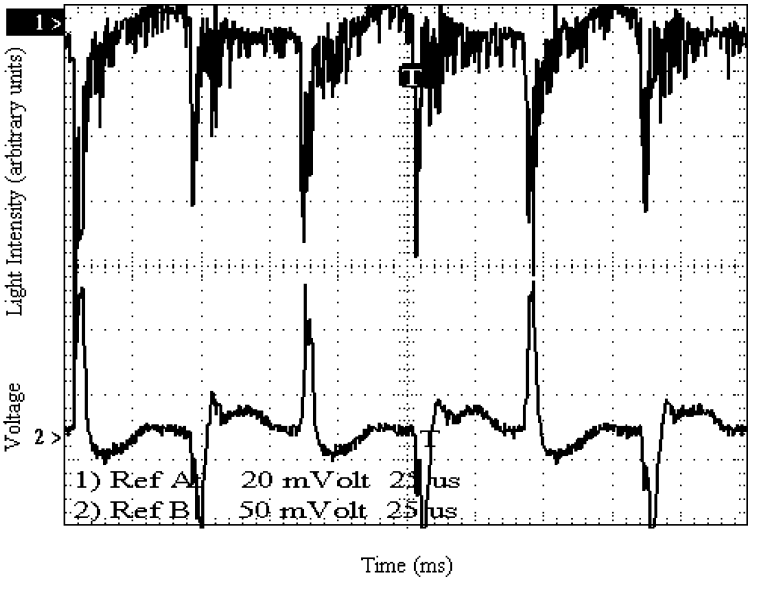

Figure 20. Light emitted and current pulse for an atmospheric air plasma.

with accurate determination of respective species densities, in order to build an ever-increasingly accurate profile of species gain within an atmospheric plasma.

5. Conclusion

The evolution of charged species in atmospheric dielectric barrier discharges in air has been modeled using existing methods coupled with previously unconsidered atmospheric reactions. An overall limit for species densities has been estimated and equations have been derived to validate this theory. The species densities increase according to an exponential rule, which can be seen from the graphs in the preceding section. The individual treatment of each time step results in an accurate model of the evolution of species densities, which can be summed to show the overall densities

https://doi.org/10.1017/S0022377808007204 Published online by Cambridge University Press

after multiple microdischarges. Due to the fact that dielectric barrier discharges typically last for times of the order of nanoseconds and given that this system has been in operation for a relatively long time (upwards of 0.1 μs), it is reasonable to expect that a high species density for both types of charged particles could exist after this time.

Acknowledgements

The authors would like to thank John Harris for his invaluable help. This work is supported by a Enterprise Ireland under project ref. No. CFTD/2004/305 (SteriPlas), under the Irish Government National Development Plan 2000–2006, which was part-financed by the European Union ERDF.

References

[1] Borcia, G., Anderson, C. A. and Brown, N. M. D. 2003 Dielectric barrier discharge for surface treatment: application to selected polymers in film and fibre form. *Plasma Sources Sci. Technol.* **12**, 335–344.

[2] Cernakova, L., Kovacik, D., Zahoranova, A., Cernak, M. and Mazur, M. 2005 Surface modification of polypropylene non-woven fabrics by atmospheric-pressure plasma activation followed by acrylic acid grafting. *Plasma Chem. Plasma Process.* **25**(4), 427–437.

[3] Yousefi, H. R., Ghoranneviss, M., Tehrani, A. R. and Khamseh, S. 2003 Investigation of glow discharge plasma for surface modification of polypropylene. *Surf. Interface Anal.* **35**, 1015–1017.

[4] Golubovskii, Yu. B., Maiorov, V. A., Behnke, J. and Behnke, J. F. 2002 Influence of interaction between charged particles and dielectric surface over a homogeneous barrier discharge in nitrogen. *J. Phys. D: Appl. Phys.* **35**, 751–761.

[5] Segur, P. and Massines, F. 2000 *Proc. 13th Int. Conf. on Gas Discharges and their Applications (GD 2000), Glasgow, 3–8 September*, p. 15.

[6] BOLSIG. KINEMA Software. Available at: http://www.siglokinema. com.

[7] Piper, L. G. 1987 Quenching rate coefficients for $N_2 a' \sum_u^-$. *J. Chem. Phys.* **87**, 1625.

[8] Atkinson, R., Baulch, D. L., Cox, R. A., Hampson Jr., R. F., Kerr, J. A., Rossi, M. J. and Troe, J. 1997 Evaluated kinetic, photochemical and heterogeneous data for atmospheric chemistry: supplement V. IUPAC subcommittee on gas kinetic data evaluation for atmospheric chemistry. *J. Phys. Chem. Ref. Data* **26**, 521–1011.

[9] Atkinson, R., Baulch, D. L., Cox, R. A., Hampson Jr., R. F., Kerr, J. A., Rossi, M. J. and Troe, J. 1997 Evaluated kinetic and photochemical data for atmospheric chemistry: supplement VI. IUPAC subcommittee on gas kinetic data evaluation for atmospheric chemistry. *J. Phys. Chem. Ref. Data* **26**, 1329–1499.

[10] Person, J. C. and Ham, D. O. 1998 Removal of SO_2 and NO_x from stack gases by electron beam irradiation. *Radiat. Phys. Chem.* **31**, 1–8.

[11] Ikezoe, Y., Matsuoka, S., Takebe, M. and Viggiano, A. 1987 *Gas Phase Ion-Molecule Reaction Rate Constants Through 1986*. Tokyo: Ion Reaction Research Group of The Mass Spectroscopy Society of Japan.

[12] Atkinson, R., Baulch, D. L., Cox, R. A., Hampson Jr., R. F., Kerr, J. A. and Troe, J. 1989 Evaluated kinetic and photochemical data for atmospheric chemistry: Supplement III. IUPAC subcommittee on gas kinetic data evaluation for atmospheric chemistry. *J. Phys. Chem. Ref. Data* **18**, 881–1097.

[13] Mirokin, Y. and Mallard, G. 1998 *The NIST Chemical Kinetics Database*.

[14] Tsang, W. and Hampson Jr., R. F. 1986 Chemical kinetic data base for combustion chemistry. Part I. Methane and related compounds. *J. Phys. Chem. Ref. Data* **15**, 1087–1279.

[15] Mukkavilli, S., Lee, C. K., Varghese, K. and Tavlarides, L. L. 1988 Modelling of the electrostatic corona discharge reactor. *IEEE Trans. Plasma Sci*. **16**, 652–660.

[16] Baulch, D. L., et al. 1994 Evaluated kinetic data for combustion modeling. Supplement I. *J. Phys. Chem. Ref. Data* **23**, 847–848.

[17] Atkinson, R. 1997 Gas-phase tropospheric chemistry of volatile organic compounds: 1. Alkanes and alkenes. *J. Phys. Chem. Ref. Data* **26**, 215–290.

[18] Tsang, W. and Herron, J. T. 1991 Chemical kinetic data base for propellant combustion I. Reactions involving NO, NO_2, HNO, HNO_2, HCN and N_2O. *J. Phys. Chem. Ref. Data* **20**, 609–663.

[19] Eliasson, B. and Kogelschatz, U. 1991 Nonequilibrium volume plasma chemical processing. *IEEE Trans. Plasma Sci.* **19**, 6, 1063–1077.

[20] Arshak, K., Guiney, I. and Forde, E. 2007 Investigation of recombination effects in dielectric barrier discharges: a model. *Proc. 34th Int. Conf. on Plasma Science (PPPS 2007), Albuquerque, New Mexico, 17–23 June 2007*, Abstracts, 290.

[21] Smirnov, B. M. 1981 *Physics of Weakly Ionized Gases*. Moscow: Mir.

[22] Aleksandrov, N. L. and Napartovich, A. P. 1986 Effect of autoionization states of negative ions on electron diffusion in a weakly ionized plasma. *Sov. J. Plas. Phy.* **12**(9), 634–636.

[23] Croquesel, E., Gherardi, N., Martin, S. and Massines, F. 2000 *Contrib. Papers of HAKONE VII, Greifswald, 10–13 September 2000*, Vol. 1, 88.

[24] Filimonova, E. A., Amirov, R. H., Kim, H. T. and Park, I. H. 2000 Comparative modeling of NO_x and SO_2 removal from pollutant gases using pulsed-corona and silent discharges. *J. Phys. D: Appl. Phys.* **33**, 1716–1727.

[25] Forde. E. 2004 Thesis, University of Limerick.

[26] Dobele, H. F., Mosbach, T., Niemi, K. and von der Gathen, V. S. 2005 Laser-induced fluorescence measurements of absolute atomic densities: concepts and limitations. *Plasma Sources Sci. Technol.* **14**, 531–541.

[27] Eichwald, O., Yousfi, M., Hennad, A. and Benabdessadok, M. D. 1997 Coupling of chemical kinetics, gas dynamics, and charged particle kinetics models for the analysis of NO reduction from flue gas. *J. Appl. Phys.* **82**(19), 4781–4794.